Soil Processes, Pedofeatures and Microscale Metal Distributions: Relevant Study of Contaminant-Dynamics Calls for Pedology-Based Soil-Depth Sampling Strategies

Folkert van Oort, Eddy Foy, Jérôme Labanowski, Sophie Leguédois, Toine Jongmans

soil systems

MDPI

Article

Soil Processes, Pedofeatures and Microscale Metal Distributions: Relevant Study of Contaminant-Dynamics Calls for Pedology-Based Soil-Depth Sampling Strategies

Folkert van Oort [1,*], Eddy Foy [2], Jérôme Labanowski [3], Sophie Leguédois [4] and Toine Jongmans [5]

1 INRA-AgroParisTech, UMR 1402 EcoSys, Soil Ecotoxicology, RD10, F-78026 Versailles CEDEX, France
2 CEA-CNRS, UMR 3685 NIMBE/LAPA, 91191 Gif-sur-Yvette CEDEX, France; eddy.foy@cea.fr
3 CNRS/Université de Poitiers, UMR IC2MP 7285, ENSIP, 1, rue Marcel Dore, F-86073 Poitiers CEDEX 9, France; jerome.labanowski@univ-poitiers.fr
4 INRA, LES, UMR 1120, F-54505 Vandœuvre-lès-Nancy, France; sophie.leguedois@univ-lorraine.fr
5 Wageningen University Research, Landscape Centre, P.O. Box 47, 6700 AA Wageningen, The Netherlands; toinejongmans@gmail.com
* Correspondence: folkert.van-oort@inra.fr; Tel.: +33-130-833-251

Received: 18 December 2017; Accepted: 13 March 2018; Published: 14 March 2018

Abstract: Short-term variations of soil conditions affect the form, mobility and bioavailability of metal pollutants. Released metals migrate toward depth where they are intercepted or precipitate, leading to variable spatial metal distribution patterns, at a macro-, meso- and microscale. Studies at a mesoscale give access to trace metal (TM) associations induced by pedological processes. Although scarcely documented, such meso-scale studies represent an essential step for relevant environmental risk assessment, halfway between field- and molecular-scale investigations. We argued for such approach by performing optical microscopy and micro-X-ray fluorescence on thin sections from two soils, contaminated either by industrial zinc-smelter waste or by urban wastewater. Consistent correlation between key indicators of pedological processes (Fe, Mn, and Ca) and trace metals (Zn, Pb, and Cu) on some 20 elemental maps of TM-hosting soil constituents and pedofeatures reveal distinct coinciding localizations, illustrating TM-accumulation via interception or (co)-precipitation processes. Micromorphological interpretation of characteristic pedofeatures in subsurface horizons (crystals, argillans, ferrans, and mangans) containing significant amounts of TM provide valuable insight into the contaminant dynamics in terms of lixiviation, colloidal transport, redox conditions, or fungal activity. Our mesoscale approach stresses the importance of pedology-based sampling strategies, instead of systematic soil-depth sampling, for soil contamination research in natural ecosystems.

Keywords: soil processes; soil horizons; metal pollutants; micrometer scale patterns; pedofeatures; optical microscopy; micromorphology; micro-X-ray fluorescence; iron; manganese; elemental correlation

1. Introduction

In soils, the fate of TM depends to a large extent on the chemical composition and weatherability of contaminant particles, on the presence of soil host-components and their affinity towards TM and on the stability of such associations. In industrial dust fallout generated by metal smelters, TM occur as sulfides, oxides, or silicates, formed under high temperature conditions, but becoming rapidly unstable under humid and slightly acid soil conditions [1–3]. After chemical weathering, metals are released and either redistributed on soil constituents, or mobilized and leached out to soil depth. In agricultural soils amended with organic waste, such as urban wastewater, strong interactions of TM with organic compounds enhance more stable associations. Adapted soil management practices, such

as liming and crop residue restitution, enhance metal retention in the surface horizon, thus limiting metal transfer to depth [4]. Particularly in soil surface horizons, a wide panel of constituents competes for hosting TM via absorption, complexation, or precipitation processes: organic matter, phyllosilicates, iron/manganese oxides, dissolved salts, carbonates, phosphates, charcoal, etc. Accordingly, the spatial distribution of TM in topsoil is complex, with localized TM-concentration hotspots randomly occurring in a groundmass with more moderate TM concentrations. The latter TM distribution generally designs a network that closely reflects TM associations with the fine (f) soil fraction (the clay-humus complex), in relation to coarse (c) grains: the c/f related distribution pattern [5]. The awareness of such heterogeneous TM distribution patterns in contaminated soils is crucial for environmental research at a molecular scale.

Physical, chemical and biological processes in arable soils influence the stability of TM associations in the pollution source compounds. A part of the mobilized metals is released and transferred, via the soil solution or by living organisms into deeper soil horizons. In soil solution, hydrated trace metals display ion-exchange properties with negative charges of clay minerals and oxides, as do alkaline earth cations [6]. However, TM may also move in the form of finely divided colloids, associated to organic or mineral phases. Such associations are only little affected by electrochemical charges, but more by local physicochemical conditions [7]. In subsurface horizons, the effects of anthropogenic homogenization by mechanical disturbance are strongly reduced and the influence of biological activity decreases. The fate of downward moving micropollutants depends more on specific soil characteristics (soil nature, structure, hydrodynamics): the interception of TM via sorption or their precipitation is closely linked to soil water transport in large pores, concomitantly with dissolved or colloidal soil matter. From the surface of these pores, wetting and drying cycles may promote diffusion of TM into the soil groundmass. Consequently, contrasted distributions of TM concentrations are often a characteristic of subsurface horizons with preferential occurrences in discrete soil fabrics [8]. Such great spatial variability at a macro-, meso-, and microscale of soil fabrics and the implication for TM accumulations is well-known to pedologists, but frequently ignored by other geoscientists [9–12]. Nowadays, an increasing number of studies are based on bulk samples collected at systematic soil depths that do not consider soil variability, nor explain and support the strategy of soil sampling that was used (c.f [1]).

Downward migration of TM cannot always be judged from a straightforward comparison of total metal concentrations in successive soil horizons [12]. In subsurface horizons, localized metal accumulations in discrete soil fabrics are valuable indicators for the migration of TM, highlighting the interception of TM by reactive soil phases or their co-precipitation. In soil micromorphology, such "*discrete soil fabric units recognizable from adjacent groundmass material by a different concentration in one or more components, or by a different internal fabric*" [5] are called pedofeatures. They are key indicators for current or past soil forming processes and for changing land use or soil management practices [13]. In addition, pedofeatures are often composed of finely divided, chemically reactive soil phases and act pre-eminently as a sink of TM. In many contaminated soils, their distribution patterns coincide with localized TM hotspots [8,14–18]. Due to their small size (≈20 µm to some millimeters), pedofeatures are generally difficult to examine on hand-samples in the field, but their presence may be suspected due to distinct colors of natural pigments (iron, manganese, organic matter). The morphology and nature of in situ pedofeatures can be studied by optical polarizing microscopy on soil thin sections and their chemical composition, in particular of major elements, by scanning electron microscopy using energy dispersive spectroscopy (SEM-EDS). The latter technique also may provide information on trace-element contents [14,19,20] but its use is often restricted, due to high detection limits. Micro X-ray fluorescence (µ-XRF) can be performed at ambient room conditions to map sub-millimeter-sized trace-element distribution patterns on thin sections, owing to lower trace-metal detection limits. Combined optical microscopy and submicroscopic analytical techniques helps identifying distinct "TM-soil constituent" hotspots, and interpreting soil processes implied in contaminant dynamics. Study on TM distributions at a µm to mm- scale is an essential step prior to molecular-scale studies [21].

Our work aimed at demonstrating the relevance of such halfway study-scale approach, as an intermediate step between the field-scale and molecular-scale speciation techniques, for providing comprehensive insight into the fate of metal contaminant dynamics. The overall goal was to show a series of heterogeneous but well-organized distribution patterns of metal trace elements as a result of specific soil processes and to advocate for the use of pedology-based sampling strategies for environmental risk assessment studies on contaminated soils. Here, we performed optical microscopy and submicroscopic analytical techniques on thin sections made from undisturbed soil samples collected in A, B and C horizons in two soils under arable land use, contaminated either by temporary disposal of zinc-smelter waste (Site 1), or by centennial irrigation with urban wastewater (Site 2). Soil constituents, organization and pedofeatures were optically identified and elemental maps of K, Ca, Fe, Mn, Cu, Zn and Pb (and occasionally of P, Ni, and Cr) were made by μ-XRF for about 20 studied features. Since a full presentation of all patterns would be too voluminous here, we first present an example of elemental mappings for each soil, and then restrict the presentation of results to elemental correlation between key major element indicators of soil processes such as Fe, Mn, Ca, and to a lesser extent K, and the main trace metal pollutants (Zn, Pb, and Cu). The micromorphology of pedofeatures and related metal distribution patterns are then discussed in terms of specific soil processes involved in TM dynamics.

2. Materials and Methods

2.1. Site and Soil Description

Site 1 was selected on the base of extensive soil survey on agricultural and forest soils carried out in a 3500 ha perimeter around a former non-ferrous metal smelter plant (1901–1968), NW of Valenciennes (northern France). Several zinc smelter plants were active in northern France during the 20th century, leading to local severe soil contamination by Zn, Pb and Cd [22,23]. Their activity engendered severe soil pollution of land in the vicinity, but atmospheric deposition of fine industrial dust may affect tens to hundreds of km [1]. In the study area, industrial waste disposal and dissemination of airborne metal fallout led to an individualization of four sectors polluted to different degrees: industrial waste land, backfilled with ore residues and scoria [23], metallophyte grassland that developed at the location of a former industrial waste belt, agricultural and forest soils receiving mainly atmospheric fallout [24–26], as well as localized point-source pollution sites [14]. The selected study soil Site 1 is located in an arable field, at the center of an ancient entry lane to a bunker of World War II, temporarily paved with solid industrial waste, which has been removed at the end of the war. In the field, crop growth is strongly limited at the location of the former lane, but shows normal growth at only 10-m distance (10–15 maize-rows). We opened a soil pit until 1.5-m depth in the center of the former lane, which allowed good representativeness of soil sampling. We collected bulk samples (several kg) in all soil horizons and layers, based on morphological criteria (Table 1). Additionally, ten undisturbed soil samples were collected in hard cardboard boxes (7.5 cm × 7.5 cm × 4 cm). The soil, developed in the Tertiary glauconite-rich Ostricourt sand formation was classified by [14] as a Eutric Gleyic Cambisol [27]. The soil had a nearly neutral pH, was loamy-sand textured, and its exchange complex was saturated at all depths. The Ap1 horizon displayed notable Zn, Pb, and Cu contents. Beneath the Ap1, TM concentrations increased 1.5 to two-fold in the compacted Ap2 layer. In underlying horizons, concentrations of Pb and Cu decreased more rapidly than of Zn.

Site 2 was located ≈20 km NW of Paris (France) in food crop production area, where urban wastewater was recycled via flooding irrigation. Discharge of urban wastewater is a worldwide practice, used to resolve water-shortage, favor fertilization benefits, promote low-cost filtering of wastewater, or produce water demanding crops. However, long-term irrigation of agricultural land with urban wastewater may alter soil quality and often introduces large amount of mineral and organic micropollutants [28,29]. In the study area, average doses of 2000 mm/year were applied since the end of the 1890s [30], leading to a strong accumulation in the surface horizon of urban

organic matter and TM (mainly Zn, Pb, Cu and Cd [4]) as well as pharmaceutics [31]. Soils were sandy textured in the surface Ap and eluvial E horizon, and a clayey-sand textured Bt horizon overlying either carbonated glauconite sand (Cs) or fragmented hard limestone (Cc). Selected characteristic soil data for Site 2, determined on bulk samples collected in several large soil pits, are presented in Table 2. For thin section preparation, a total of more than 30 undisturbed samples were also taken in all soil horizons. The Ap horizon contained up to ≈5% of organic matter, unusual for such sandy arable soils, but also large TM contents (Table 2) and secondary lime precipitates resulting from wastewater evaporation. Metal-concentration profiles point to the migration of Zn, Cd and Cu towards depth, and Zn-interception in the Bt horizon. The geological substratum and the soil cover underwent strong cryoturbation during the late Pleistocene [32]. In such polygonal soils, additional soil survey was performed in deep trenches giving access to the morphology and thickness of soil horizons [32], and revealed deep bending of the clay-rich Bt horizon into the carbonated substrate, until 1.5–2-m depth. In these soil trenches additional bulk sampling and collecting of about 50 undisturbed samples guaranteed the representativeness of samples. Soils were classified as Haplic Luvisols [27], but locally strong bleaching of the E horizon ascribed to intensive percolation of wastewater added albic characters [18].

Table 1. Selected physical and chemical data for the soil of Site 1 (arable land under temporary disposal of metal smelter waste). BD: bulk density; clay: <2 µm; sand: 50–2000 µm; total metal contents measured by ICP-MS after HF-HCl-HClO4 digestion; S/CEC: basic cation saturation of the exchange complex (all data from [14]).

Hor	Depth	Org. C	BD	Clay	Sand	pH	S/CEC	Ca	Fe	Mn	Zn	Pb	Cu
-	cm	g/kg	kg/m^3	g/kg		-	-	g/100g			mg/kg		
Ap1	0–30	18	1520	76	688	6.8	sat	0.30	1.05	153	1046	362	56
Ap2	30–35	22	1700	76	699	7.2	sat	0.22	1.40	291	2635	517	113
AB	35–45	3	1650	77	673	7.3	sat	0.14	1.03	143	940	21.5	11
B1	45–60	2	1680	85	657	7.0	sat	0.19	1.07	406	259	14.6	8.6
B2g	60–80	<1	1550	96	631	6.7	sat	0.17	1.25	660	86	11.1	6.7
BCg	80–120	<1	1550	166	639	6.6	sat	0.22	1.91	461	53	12.3	6.7
C1g	120–150	<1	1650	124	819	6.1	sat	0.15	1.55	171	28	11.9	6.0

Table 2. Selected physical and chemical data for the soil of Site 2 (arable land under centennial wastewater irrigation). BD: bulk density; clay: <2 µm; sand: 50–2000 µm; -: not relevant; total metal contents measured by ICP-MS after HF-HCl-HClO4 digestion; (data compiled after [4,18]).

Hor	Depth	Org. C	BD	Clay	Sand	pH	$CaCO_3$	Ca	Fe	Mn	Zn	Pb	Cu
-	cm	g/kg	kg/m^3	g/kg		-	%	g/100g			mg/kg		
Ap	0−40	31.0	1250	91	767	7.1	43.9	2.25	1.25	161	1130	607	329
E	40−55	1.3	1730	41	877	7.3	<1	0.12	0.56	40	246	7.9	44.6
Bt	55−75	2.4	1610	206	717	7.5	2.5	0.40	2.49	118	463	11.8	23.3
B/C	75−90	1.5	1570	39	827	8.3	162	5.64	1.06	118	171	7.3	27.1
Cs	90−120	1.4	1710	108	759	8.7	382	9.68	0.75	160	27	4.0	5.5
Cc *	>60	1.7	-	196	597	8.6	573	13.9	0.56	81	52	3.8	10.1

* Samples collected at some meters distance from the study site, where fragmented hard limestone occurred close to the soil surface.

2.2. Methods

Undisturbed soils samples were collected in hard cardboard boxes (7.5 cm × 7.5 cm × 4 cm), air-dried and impregnated with polyester resin before cutting and polishing to 30 µm thickness to produce thin sections [33]. The nature, morphology and organization of coarse soil constituents and the fine plasma were studied with a petrographic Nikon Eclipse E400 polarizing light microscope using the terminology currently employed in soil micromorphology [5]. Micrometer scale distribution

maps of major (Fe, Ca, K, Ti, P, and Mn) and trace elements (Ni, Cr, Zn, Cu, and Pb) were made on selected parts of thin sections by μ-XRF with a Rigaku RU-200B rotating anode X-ray generator. The monochromatized beam delivered by a molybdenum anode (main Kα radiation at 17.5 keV) provided a Kα spectral purity >97% and Kβ contamination <0.3%. Beam-focusing with a spot-size of 50 μm × 30 μm at the surface of samples was performed using a Xenocs FOX 2DMo 25-25P collimating multilayer optics. Runs were made at 21 mA and 55 kV, with dwell times ranging from about 100 to 1000 s per point, depending on TM concentrations and the analyzed surface. Samples were placed at 45° of the X-ray beam and fluorescence spectra were collected at 90° through an AXAS Vitus SDD (10 mm^2 of active surface) Ketek detector. An in-house program made in Visual Basic 6.0 was used to synchronize the samples displacement (step size Δx = 50 μm, Δy = 30 μm) with motorized linear translation stages and the spectra acquisition recorded with GENIE-2000 program. Elemental distribution maps were generated using Origin©. Non-normality of element distributions was checked (Shapiro–Wilk) for all maps and Spearman correlation (ρ) was used to assess statistic correlation between pairs of elements.

3. Results

3.1. Site 1: Zinc-Smelter Waste Contamination

3.1.1. Micromorphology in A, B and C Horizons

Optical microscope images of characteristic constituents, organizations and pedofeatures, involved in metal retention in soils, are presented in Figure 1. Millimeter-sized waste fragments containing well-crystalized metal-bearing minerals such as hardystonite, anglesite, willemite and franklinite (determined by analytical electron microscopy and X-ray diffraction) or more amorphous phases, frequently occurred in the Ap1 horizon (Figure 1a). The Ap1 groundmass also contained many coarse and fine fragments of particulate organic matter (POM), phosphates, charcoal, and small iron oxides. The fine groundmass occurred as small aggregates between large skeleton grains (enaulic c/f-related distribution pattern) (Figure 1b). Locally, in and around waste fragments, many fine (1–5 μm), yellowish spherical bodies were observed (Figure 1c). At high magnifications and in cross-polarized light, such crystal pedofeatures exhibited a central black extinction cross, perpendicularly oriented to the reticule, referred to as spherulites [34]. Similar crystals also were observed as clusters isolated in the quartz groundmass (Figure 1d), or on large POM fragments (Figure 1e), suggesting that their precipitation was favored by fungal activity. The compacted Ap2 horizon, displayed a platy microstructure with sub-horizontal cracks. The void walls showed dark-brown impregnations (hypocoatings) (Figure 1f). In AB, B1 and B2g horizons, numerous coarse, silt-sized, red to reddish-brown spherulites were observed (Figure 1g), preferentially located around voids (channels and vughs) but also away from voids in the groundmass. In the field, these accumulations were identified as localized, intense reddish mottling, between about 35 and 75 cm depth, and hence initially interpreted as a result of temporary hydromorphic soil conditions. Their abundance was maximal at about 60 cm depth, where their coalescence (Figure 1h) occasionally formed continuous pure iron coatings. Such red spherulites clearly showed a black extinction cross and a concentric morphology, visible both in cross-polarized as well as in plain polarized light. The colors and morphology suggest a crystalline goethite composition [35]. At depths >75 cm, such rounded, reddish iron-oxide crystals still occasionally occurred, but they did no longer display the typical spherulite morphology. Moreover, mm-sized black iron nodules were present. In the C1g horizon, translucent clay coatings occurred in large pores, frequently covered by distinct, pure iron coatings (Figure 1i). The two types of coatings were separated by a sharp boundary. The iron coatings showed a botryoidal outer surface (Figure 1j) and a crystal fabric with crystallization axes perpendicular and radially oriented to the wall of the void. Such fabrics and boundaries are ascribed to neoformation of iron oxyhydroxides, often goethite coatings [35] resulting from precipitation of iron compounds out of a percolating soil solution.

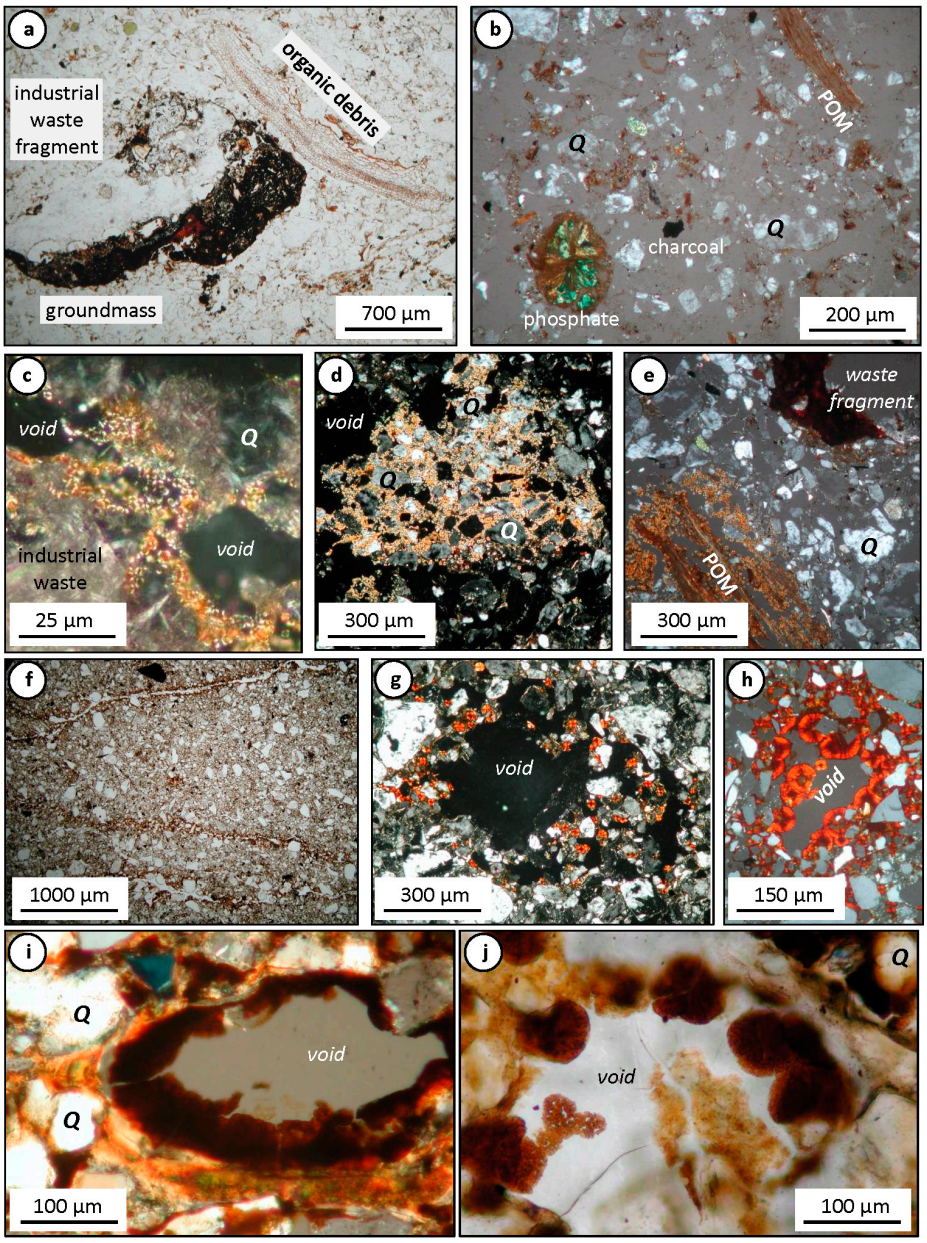

Figure 1. Micromorphology of soil constituents and pedofeatures in a soil under temporary zinc-smelter waste (Site 1): (**a**) frequently occurring coarse metal bearing particles in the surface Ap1 horizon: industrial waste fragments, organic plant debris; (**b**) phosphates, charcoal fragments in the groundmass; (**c**) neoformed small (1–5 µm), yellow to yellow-orange spherical bodies in waste fragments; (**d**) as clusters in the quartz groundmass, or (**e**) precipitated on organic fragments in the vicinity of waste fragments; (**f**) platy structure in the Ap2 horizon with dark hypo-coatings along cracks; (**g**) red, coarse-silt-sized spherulite crystals in, and around large voids in the B1 horizon; (**h**) local coalescing of red spherulites to form pure iron coatings; (**i**) distinct pure iron coating, juxtaposed over continuous oriented, translucent clay coatings on large void walls in the C1g horizon; and (**j**) displaying at high magnification botryoidal outer-surfaces. Photos in plain polarized light (**a**,**f**,**j**), other pictures in (half) crossed polarized light. Q = quartz; POM = particulate organic matter.

3.1.2. Contrasting Hecto-Micrometer Scale Metal Distributions in the Surface Horizon

In the Ap1 horizon, an almost 2 mm^2 surface of the groundmass, centered on a ≈300-µm-sized zinc-smelter slag particle (1), was analyzed in thin sections by µ-XRF (Figures 2a and 3a). Despite

a residence time of at least 50 years, the waste fragment still demonstrated highly localized concentrations of Fe, Zn and Pb (Figure 2b), but also of Ca and Cu. An adjacent plant root (2), distinctly materialized by Mn, also contained Zn and Cu. In POM fragments (3), clear accumulations of Zn and Pb were revealed, but Cu was not detected. Zinc was also detected in iron-oxide particles (4). Opaque charcoal particles (5) were clearly materialized on the Zn and Pb, but poorly on Cu maps. Lastly, the distribution pattern of the fine soil fraction (plasma) in the Ap1 horizon (6) designed a network of moderate concentrations that surround the large quartz grains, notably on Zn and Fe maps (Figure 2a). Because of such heterogeneous TM distributions, linear regression correlation applied on the whole maps (Figure 2c) was largely influenced by high Fe, Ca, Zn, Pb, and Cu contents in the waste particle. Most correlation graphs showed effects of multiple metal locations: (i) for Zn/Mn, a large proportion of Zn was strongly correlated with Mn in the plant root spot, but Zn also occurred in the groundmass without Mn; and (ii) the Zn/Cu correlation illustrated their concomitant occurrence in the waste fragment, but Cu was more present in organic plant debris and charcoal than Zn. Figure 2c illustrates the non-normality of element distributions, supporting Spearman's test for assessing elemental correlation (Table 3).

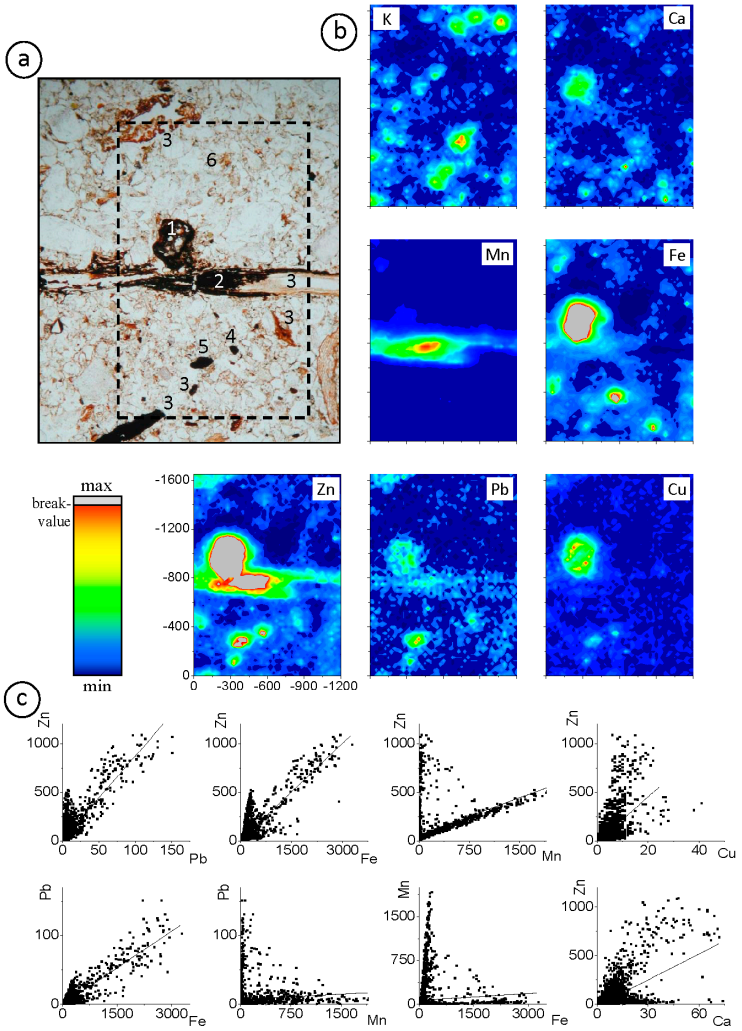

Figure 2. Micro X-ray fluorescence analyses in the Ap1 groundmass of a soil under temporary disposal of zinc-smelter waste: (**a**) optical microscopy image of the analyzed 1200 × 1850-µm area: (1) industrial slag fragment; (2) plant root; (3) POM particles; (4) iron oxide; (5) charcoal; and (6) distribution network of the fine soil fraction (plasma); (**b**) spatial distribution maps of K, Ca, Mn, Fe, Zn, Pb and Cu; and (**c**) linear regression lines.

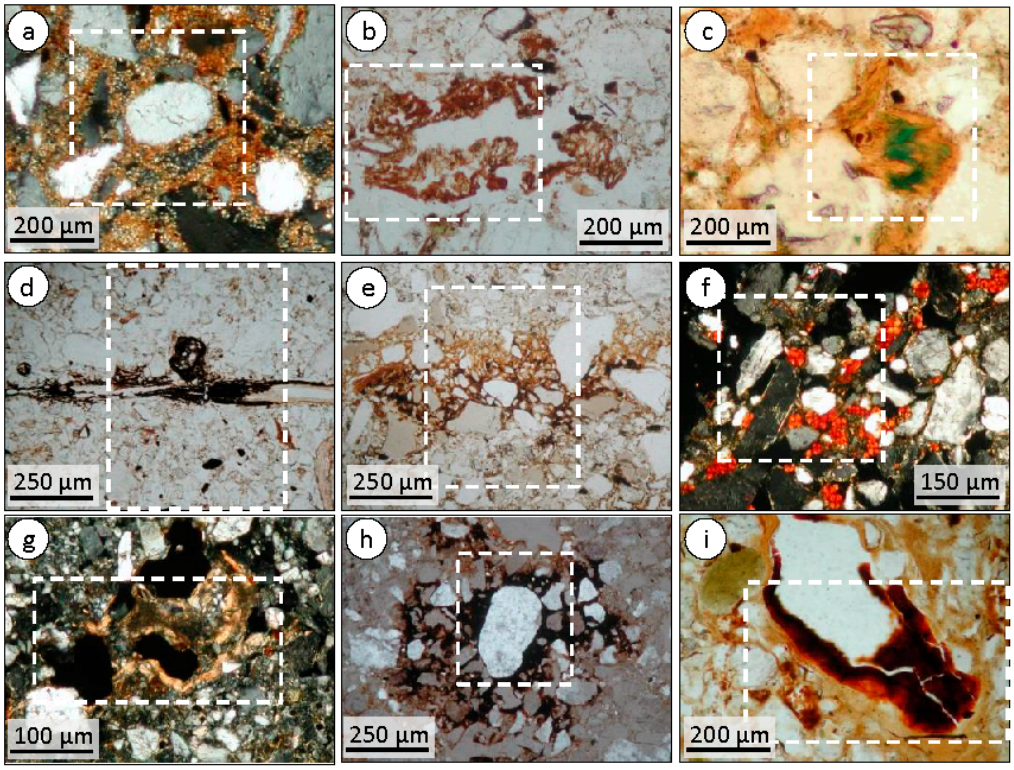

Figure 3. Analyzed surfaces of thin sections by µ-XRF in A, B and C horizons of Site 2. Description of the focused constituents and pedofeatures and Spearman correlation values are assembled in Table 3): (**a**) Ap1 horizon, yellow spherulites (40,000 µm^2); (**b**) organic debris (14,000 µm^2); (**c**) iron phosphate (40,000 µm^2); (**d**) Ap1 horizon, groundmass (1.89 mm^2); (**e**) Ap2 horizon, dark hypocoatings (357,000 µm^2); (**f**) AB, B1 horizon, red spherulites (82,500 µm^2); (**g**) B1, B2g horizon, clay-iron coating (45,000 µm^2); (**h**) B2g horizon, manganese nodule (270,000 µm^2); and (**i**) C1g horizon, pure iron coating (216,000 µm^2).

3.1.3. Elemental Correlation Analyses on Selected Features of A, B, and C Horizons

In the Ap1 horizon of Site 1, remarkably high correlation was found among Zn, Pb and Cu as well as between these metals and Fe, Mn and Ca for yellow spherulites occurring as fine crystals precipitated around large quartz grains (Figure 3a): ρ was always $\geq$0.8, often >0.9 and reached values as high as 0.98 for Zn and Pb with Fe and Mn (Table 3). Such strong correlation was also found for yellow spherulites occurring within slag particles [14], as precipitations on POM fragments or in the groundmass at the contact with waste fragments (Figure 1c–e). These findings strongly suggest that these crystals precipitate from concentrated solutions seeping out of weathering waste fragments and hence represent the major source of heavy metal in the Ap1 horizon. In broad literature, organic debris and phosphates were often reported as major sinks for TM soils [36,37]. Micro-XRF analysis performed on an organic debris (Figure 3b) highlighted strong correlation between Zn, Pb and Fe and a $\rho_{Zn/Ca} > 0.8$ (Table 3); an iron-phosphate particle (Figure 3c) displayed strong correlation for Pb with Fe and for Zn with Mn ($\rho > 0.9$). The correlation in individual constituents was clearly larger than for a global analysis of the groundmass (Figures 2 and 3d, Table 3).

Table 3. Site 1: Spearman correlation (ρ) between major (Fe, Mn, Ca) and trace (Zn, Pb, Cu) elements obtained by µ-XRF analyses on selected areas of soil thin sections (Figure 3). 3a–3d: Ap surface horizon, 3e–3i: subsurface horizons. ■: $\rho \geq 0.9$; ■: $0.8 < \rho < 0.9$; ■: $0.7 < \rho < 0.8$, values: $0.5 < \rho < 0.7$; -: $\rho < 0.5$. The number of measure points ranged from about 80 (b) to more than 3200 (d).

Photo	ρ Major/Major			ρ Trace/Trace			ρ Zn/Major			ρ Pb/Major			ρ Cu/Major			
n°	Fe/Mn	Fe/Ca	Ca/Mn	Zn/Pb	Zn/Cu	Cu/Pb	Zn/Fe	Zn/Mn	Zn/Ca	Pb/Fe	Pb/Mn	Pb/Ca	Cu/Fe	Cu/Mn	Cu/Ca	Additional Remarkable Correlation
3a	0.98	0.94	0.95	0.98	0.80	0.82	0.98	0.96	0.91	0.98	0.98	0.93	0.80	0.84	0.80	Fe/P: 0.57
3b	-	0.52	-	0.87	0.55	-	0.80	-	0.76	0.84	-	0.61	-	-	0.58	
3c	0.73	0.55	-	0.63	0.68	0.60	0.67	0.92	-	0.94	0.66	-	0.54	0.64	-	
3d	-	0.55	-	0.61	0.59	-	0.73	0.59	-	0.60	-	-	-	-	-	
3e	0.57	-	-	-	-	-	0.81	0.85	-	-	-	-	-	-	-	
3f	0.89	0.56	0.61	-	-	-	0.94	0.88	-	-	-	-	-	-	-	Ti/K: 0.82; Ca/K: 0.74
3g	0.70	-	0.56	-	-	-	0.90	0.68	-	-	-	-	-	-	-	Fe/Ti: 0.84; Zn/Ti: 0.82; Mn/Ti: 0.71;
3h	0.58	-	-	-	-	-	0.59	0.78	-	-	-	-	-	-	-	
3i	-	0.66	-	-	-	-	-	-	-	0.78	-	-	-	-	-	K/Ti: 0.67

In the compacted Ap2 horizon, iron- and manganese-rich hypocoatings (Figure 3e) along the horizontal cracks (Figure 1f) demonstrated strong correlation for Zn with Mn ($\rho_{Zn/Mn}$ = 0.85) and more moderate correlation for Zn and Pb with Fe ($\rho_{Zn/Fe}$ = 0.81, $\rho_{Pb/Fe}$ = 0.61). In the underlying AB and B1 horizons, the numerous red spherulites (Figure 3f) showed remarkable strong correlation between Zn, Fe and Mn ($\rho_{Zn/Fe}$ = 0.94, $\rho_{Zn/Mn}$ = 0.88), and moderate correlation between Mn and Ca ($\rho_{Ca/Mn}$ = 0.61) (Table 3). In the B1 and B2g horizons, µ-XRF analyses were performed on pedogenetic yellowish-orange translucent clay-iron coatings lying around skeleton grains and in biopores and vughs (Figure 3g). Strong correlation was observed between Zn and Fe, lower correlation between Fe and Mn, but also good correlation between Zn and Ti (Table 3), the presence of titanium illustrating its localization in phyllosilicates. In the B2g horizon, accumulations of manganese occurring as Mn-nodules frequently occurred (Figure 3h). Micro-XRF analyses showed good correlation between Zn and Mn. In the Cg horizon, contemporary pure iron coatings (ferrans) overlying pedogenetic ferri-argillans in biopores (Figure 3i) showed close-similar Pb and Fe distribution patterns and remarkable high correlation ($\rho_{Pb/Fe}$ = 0.78) for such great soil depth (Table 3).

3.2. Site 2: Urban Wastewater Contamination

3.2.1. Micromorphology in A, B and C Horizons

Optical microscopic images of typical soil constituents, organizations and pedofeatures in soils affected by one century discharge of urban wastewater are presented in Figure 4. The surface horizon contained large amounts of POM fragments (Figure 4a, 1). The finely divided, dark-brown amorphous organic matter including many very fine calcium carbonate crystals (Figure 4b) surrounded the coarse quartz skeleton grains (chitonic c/f related distribution pattern) [5]. Many allochthonous particles, such as charcoal, plastic fragments, and occasionally industrial slag (Figure 4a, 2–4) were observed, as well as phosphates and fishbone fragments. The upper part of the E horizon displayed very little fine plasma between the sand grains (Figure 4c), but locally, fine dark-brown fibers were observed (Figure 4d) and ascribed to capillary rising of suspended fine soil particles from the clay-rich Bt horizons, issued by strong drying of the sandy surface after repetitive irrigation events [18,32]. In addition, silty-clay textured, non-translucent dusty coatings were frequently observed (Figure 4e), illustrating the downward moving of fine material out of the Ap horizon during fast rewetting after wastewater flooding. The gradual and wavy transition of the E and Bt horizon, distinguished as a 10–20-cm thick E/Bt horizon, demonstrated irregularly shaped, faint to distinct, orange-brown mottling deriving from hydromorphic processes: ferrolysis, leading to clay degradation [18,38] (Figure 4f). In the E/Bt and upper Bt horizon, large pores were often covered by crystalline pure iron coatings (Figure 4g), the iron originating from the clay destruction process. Deeper in the Bt and B/C horizons, translucent clay coatings resulting from Luvisol formation were dominant (Figure 4h). Additional remarkable features were frequent occurring dark reddish-brown particles identified as fungal pseudo-tissues (sklerotia) and cell clusters (Figure 4i–j), spatially intimately related. They were preferentially present along the boundaries of the clay-rich Bt horizon, either with the aerated sandy textured E horizon close to the soil surface, or at the contact with the porous fragmented limestone (Figure 4k) as deep as 2 m. A general blackening effect due to alteration of the fungal tissues was observed, varying form dark red and reddish-brown organ fragments with recognizable cell structures to black, opaque amorphous organic structures that occasionally formed black coatings overlying ferri-argillans on void walls. Such features were reported as Mn-reduction based fungal activity hot spots in soils with temporarily anoxic conditions [39].

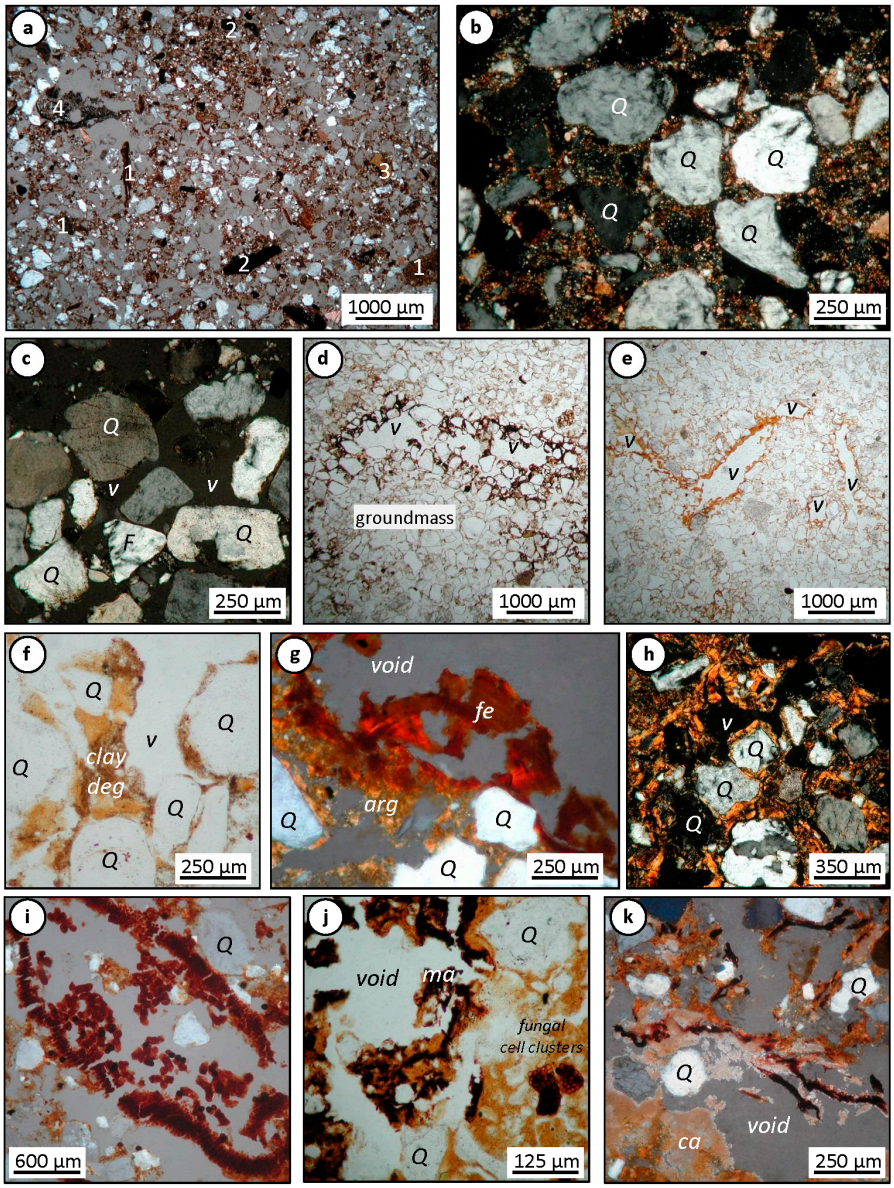

Figure 4. Micromorphology of soil constituents and pedofeatures in a soil under centenary wastewater irrigation (Site 2). The groundmass (**a**) includes: POM fragments (1); charcoal (2); plastic fragments (3); and occasional industrial waste (4); and demonstrates a chitonic distribution of the fine amorphous organic matter rich plasma with many secondary carbonate crystals around the coarse quartz grains (**b**). In the E horizon, little fine groundmass is present (**c**); hypo-coatings in the E horizons ascribed to periodically capillary rising (**d**); dusty clay coatings in the E and E/Bt horizons (**e**); pale-yellow granular clay coatings in E/Bt horizon, resulting from ferrolysis (**f**); pure, fan-like iron coatings in the E/Bt horizon (**g**); translucent clay coatings in Bt horizons (**h**); reddish tissue residues from fungal activity with recognizable cell-structures in Bt horizons (**i**); dark, opaque manganese precipitations on clay-iron coatings in a large void (**j**); and at the contact of the carbonate substrate (**k**). Photos in plain polarized light (**d**–**f**,**j**), or in (half) crossed polarized light (**a**–**c**,**g**–**i**,**k**). Q = quartz; v = void; ma = mangans; arg = clay coating; fe = pure iron coating; deg = degradation; ca = limestone.

3.2.2. Physicochemical Significance of Horizon Boundaries Regarding Metal Retention

Micro-XRF was performed on a 575 µm × 3000 µm area, centered on the Ap/E horizon boundary (Figure 5a). The Si-map (Figure 5b) illustrates a continuity of quartz grains in both horizons, whereas

the K-map underlined the occurrence of K-feldspars, as well as a more diffuse presence of K in large organic matter rich aggregates in the Ap horizon. For Fe, largest contents were found in the Ap horizon, but its presence in the E horizon attested for the presence of small amounts of fine plasma. Manganese was only little present in the Ap and E horizons. Calcium showed distinct patterns in the Ap horizon, ascribed to a coarse carbonate particle and to many fine secondary carbonate crystals in the amorphous organic matter plasma. Strikingly, immediately below the Ap/E horizon boundary, virtually no Ca was detected. The distribution patterns of Cu, Zn and Pb were fairly similar. They generally coincided with the distribution of the fine organic groundmass, but some spots with larger concentrations were associated with iron-rich components. Similar to Ca, no Pb was detected in the E horizon: the limit of Pb detection at the Ap/E boundary was abrupt. Some zinc was detected in the E horizon, with a distribution pattern comparable to Fe and K, suggesting Zn-sorption by the small amounts of clay-iron groundmass in the E horizon. In the E horizon, Cu was occasionally detected on small POM fragments, as confirmed by optical microscopy.

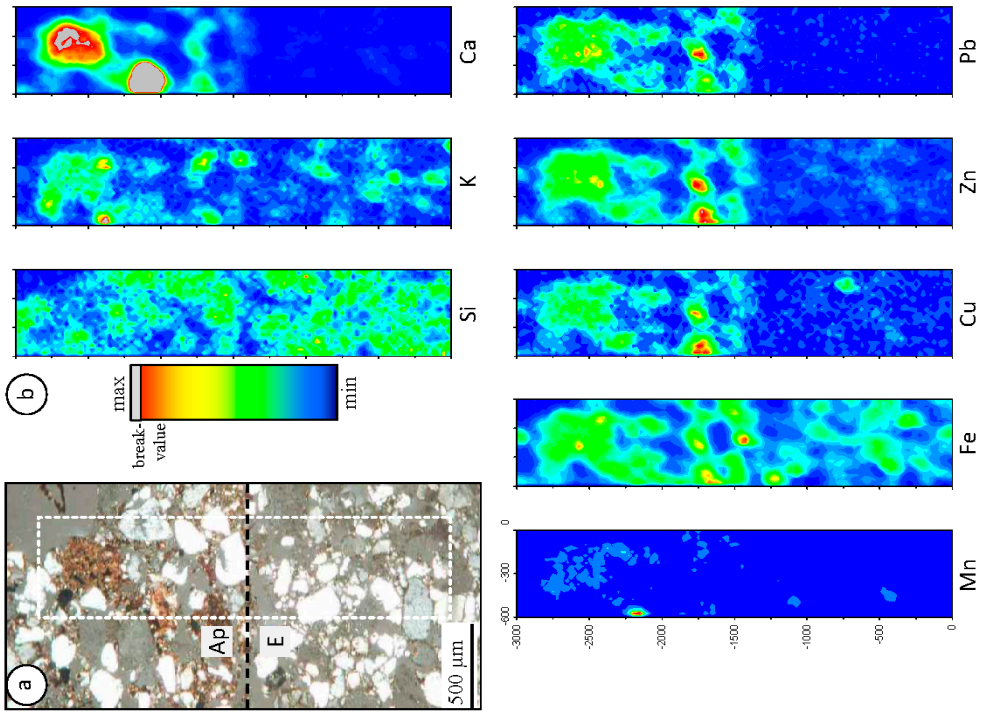

Figure 5. Micro X-ray fluorescence analyses in transition between the Ap and E horizon in the soil of Site 2: (**a**) optical microscope image of the analyzed 600 µm × 3000 µm area; and (**b**) spatial distribution maps of Si, K, Ca, Mn, Fe, Cu, Zn, and Pb.

3.2.3. µ-XRF Elemental Correlation Analyses on Selected Features of A, E, B and C Horizons

In the Ap horizon, several constituents and compounds contributed to metal retention (Table 4), in particular many large plant-debris and phosphates. A global mapping by µ-XRF in the groundmass (Figure 6a) showed fairly good correlation for Zn, Cu and with Fe and Ca as well as between Pb and Fe, notably in large organic fragments [17]. When focusing on the relative distribution of the soil plasma and skeleton grains (Figure 6b), good correlation was observed for Zn and Pb with Fe and Ca, but not for Cu, probably due to lower concentrations. This latter finding point to the preferential affinity of Cu for POM fragments [36,40,41]. Phosphates, in particular iron-phosphates (Figure 4c), demonstrated remarkable high correlation between Zn, Pb and Cu, and also some Cr (Table 4). These results underlined the high affinity of phosphate compounds for heavy metals. High correlation was observed for Zn, Pb and Cu with Fe ($\rho > 0.9$), and to a lesser extent with Mn. Copper was detected in a

calcium phosphate grain (Figure 6c), with good correlation of Zn, Pb and Cu with Ca and P (Table 4). Elemental mapping at the transition from the Ap to the underlying eluvial E horizon (Figures 5 and 6d) showed good correlation for Zn, Pb and Cu with Fe and for Zn and Pb with Ca. Correlation for almost all pairs of elements increased limiting to the lower part of the Ap horizon, whereas, in the E horizon, no more correlation was observed, apart from a $\rho_{Zn/Fe}$ of 0.75.

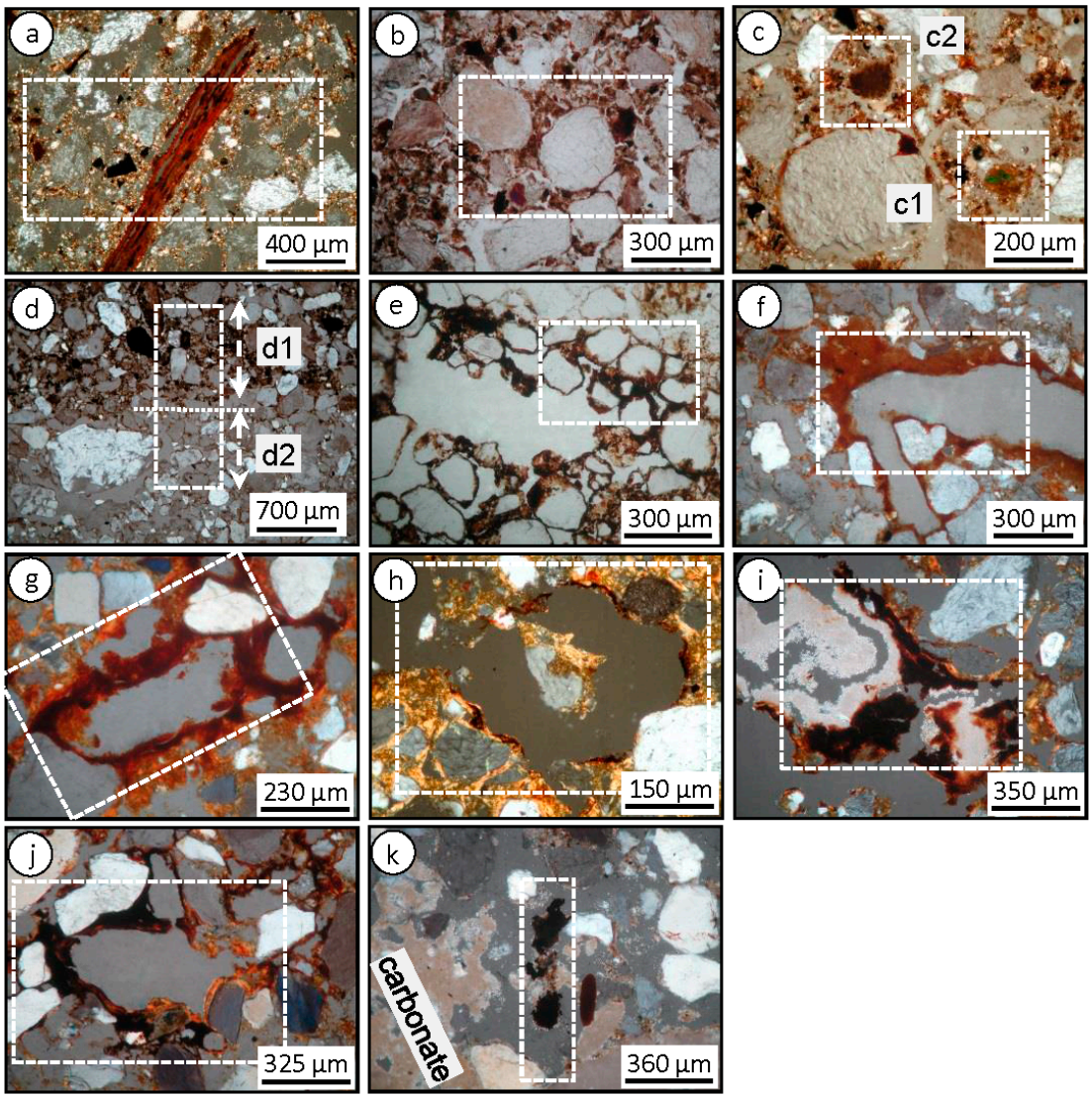

Figure 6. Analyzed surfaces of thin sections by µ-XRF in A, B and C horizons of Site 2. Description of the focused constituents and pedofeatures and Spearman's correlation values are detailed in Table 4: (**a**) Ap groundmass (656,250 µm^2); (**b**) chitonic distribution of the fine plasma around coarse sand grains (357,000 µm^2); (**c**) phosphate crystals: (c1) iron-phosphate (40,000 µm^2), (c2) calcium phosphate (61,500 µm^2); (**d**) Ap/E horizon transition (1.8 mm^2): (d1) Ap-part (960,000 µm^2), (d2) E-part (780,000 µm^2); (**e**) E horizon, capillary-rising fibers (234,000 µm^2); (**f**) E and E/Bt horizon, dust coatings (480,000 µm^2); (**g**) E/Bt horizon, pure iron coatings (330,000 µM^2); (**h**) Bt and BC horizon, clay-iron coatings (281,250 µm^2); (**i**) Bt, BC and C horizons, fungal sklerotia (720,000 µm^2); (**j**) Bt and BC horizon, manganese coatings (660,000 µm^2); and (**k**) Cs horizon, (organic) colloidal precipitates (153,000 µm^2).

Table 4. Site 2: Spearman correlation (ρ) between major (Fe, Mn, Ca) and trace (Zn, Pb, Cu) elements obtained by µ-XRF analyses on selected areas of soil thin sections (Figure 6). 6a–6d: Ap surface horizon, 6e–6k: subsurface horizons. ■: $\rho \geq 0.9$; ■: $0.8 < \rho < 0.9$; ■: $0.7 < \rho < 0.8$, values: $0.5 < \rho < 0.7$; -: $\rho < 0.5$. The number of measure points ranged from about 90 (c) to more than 3000 (d).

Photo	ρ Major/Major			ρ Trace/Trace			ρ Zn/Major			ρ Pb/Major			ρ Cu/Major			
n°	Fe/Mn	Fe/Ca	Ca/Mn	Zn/Pb	Zn/Cu	Cu/Pb	Zn/Fe	Zn/Mn	Zn/Ca	Pb/Fe	Pb/Mn	Pb/Ca	Cu/Fe	Cu/Mn	Cu/Ca	Other Remarkable Correlation
6a	-	0.76	-	0.76	0.86	0.68	0.95	-	0.74	0.75	-	-	0.85	-	0.66	
6b	-	0.79	-	0.77	0.52	0.53	0.88	-	0.76	0.80	-	0.63	0.52	-	-	
6c1	0.84	0.77	0.62	0.94	0.91	0.86	0.98	0.81	0.80	0.92	0.73	0.76	0.88	0.65	0.79	Cu/Cr: 0.70; Pb/Cr: 0.64; Zn/Cr: 0.63
6c2	0.70	0.86	0.74	0.95	0.95	0.93	0.91	0.71	0.92	0.91	0.71	0.90	0.90	0.75	0.90	Pb/Cr: 0.64; Cu/Cr: 0.62; Zn/Cr: 0.62
6d	0.65	0.65	0.57	0.78	0.80	0.73	0.83	0.62	0.84	0.61	0.53	0.82	0.69	0.52	0.76	Zn/K: 0.66
6d1	0.69	0.80	0.65	0.88	0.86	0.81	0.92	0.69	0.84	0.84	0.65	0.80	0.82	0.61	0.74	Fe/K: 0.75; Zn/K: 0.75, Pb/K: 0.70
6d2	-	0.54	-	-	-	-	0.71	-	-	-	-	-	-	-	-	
6e	0.63	-	-	-	0.75	-	0.67	0.98	-	-	-	-	-	0.77	-	Ni/Mn: 0.86; Ni/Fe: 0.62
6f	-	-	-	0.52	0.86	-	0.97	-	-	0.53	-	-	0.88	-	-	
6g	-	-	-	0.78	0.66	0.57	0.98	-	-	0.76	-	-	0.65	-	-	Fe/Ti: 0.70; Zn/Ti: 0.66
6h	-	0.98	-	-	-	-	0.94	0.60	0.94	-	-	-	-	-	-	Zn/K: 0.87; Zn/Ti: 0.88; Fe/K: 0.70
6i	0.79	-	-	-	-	-	0.86	0.95	-	-	-	-	-	-	-	Ni/Mn: 0.74; Zn/Ni: 0.71; Fe/K: 0.62
6j	0.57	-	-	-	-	-	0.66	0.82	-	-	-	-	-	-	-	Ni/Mn: 0.64; Fe/K: 0.58; Zn/K: 0.53
6k	0.72	-	-		0.65		0.72	0.66	-	-	-	-	0.75	0.68	-	Fe/Ti: 0.70; Zn/Ti: 0.67; Fe/K: 0.58

In the E horizon, bow-like dark brown fibers, ascribed to capillary rising from underlying thick clay-rich bodies (Figure 6e) contained Fe and Mn and showed outstandingly high Zn/Mn correlation (ρ = 0.98), but also correlation for Cu and Ni with Mn (ρ = 0.77 and 0.86, respectively). Dusty clay coatings in the E and E/Bt horizons (Figure 6f) showed good correlation among Zn, Pb, Cu and Fe/Ca (Table 4), consistent with their formation by illuviation of fine groundmass material from the Ap horizon. The pure iron coatings (Figure 6g) included Zn ($\rho_{Zn/Fe}$ = 0.98), but also Pb and some Cu ($\rho_{Pb/Fe}$ = 0.76, $\rho_{Cu/Fe}$ = 0.65). In Bt horizons, preferential associations of Zn with Fe, K and Ni ($\rho_{Zn/Fe}$ = 0.94, $\rho_{Zn/K}$ = 0.87, $\rho_{Zn/Ni}$ = 0.88, respectively) illustrated the interception of free Zn moving in the soil solution by negatively charged clay coatings (Figure 6h). All features related to fungal activity, predominantly observed at the boundaries between the clay-rich Bt horizon and over- or underlying more aerated E or C horizons, the reddish-brown sklerotia fragments (Figure 6i) to dark brown or black coatings (Figure 6j) demonstrated remarkably high correlation at great depth for Zn (and Ni) with Mn ($\rho_{Zn/Mn}$ = 0.95–082, $\rho_{Ni/Mn}$ = 0.74–0.64). In C horizons (Figure 6k), orange-brown organic matter precipitations were frequently observed, containing Fe, Mn, Zn, and Cu. Such deep accumulations attested for colloidal transfer of metal pollutants, precipitating at the proximity of the carbonate substrate.

4. Discussion

4.1. Relevance of Micrometer-Sized Analyses on Undisturbed Soil Samples

Frequently mentioned adjectives related to soil metal pollution problematic are "complex" and "heterogeneous". Such terms depict the great variability of soil mineral and organic constituents, but also the processes, biological activity and anthropogenic practices that affect soils. However, the combination of micromorphology and micro X-ray fluorescence, performed on thin sections made from undisturbed soil samples, demonstrates that the apparent complexity in reality expresses well-localized metal accumulations. In surface horizons, metal accumulation hotspots are most often linked to the presence of distinct organic or mineral constituents (plant residues, phosphates, charcoal, industrial waste fragments, and organo-mineral associations). Considering such variable metal distribution patterns, comprehensive insight into metal dynamics and formation of privileged "TM-soil constituent" associations demands to restrict the use of µ-XRF analyses on selected areas with one single dominant TM hosting constituent. In subsurface horizons, the metal accumulations generally coincide with specific pedofeatures. The concentrations of TM elements in pedofeatures often strongly contrast with concentrations in the surrounding groundmass. The formation of pedofeatures is intimately related to past pedogenetic processes, but also to current soil processes induced by changing land use, soil management practices, and other anthropogenic activities [13] that drive the dynamics of contemporary soil contamination. For both soils, the multitude of significant correlation for element pairs in the surface Ap horizon was strikingly contrasting with those observed in subsurface horizons (Tables 3 and 4). However, in pedofeatures at depth, some single trace/major element pairs showed remarkable high elemental correlation, sometimes even higher than in the soil surface horizon. Zinc was by far the most frequently detected TM in pedofeatures at depth, generally highly correlated with Fe, underlining its general mobility in soils. Interestingly, sudden changes of correlation in B and C horizons, i.e., Zn/Fe to Pb/Fe in Site 1 (Table 3), and Zn/Fe to Zn/Mn in Site 2 (Table 4) clearly demonstrate the role of specific soil processes on contaminant dynamics at great depth.

One limitation of our combined optical microscopy and µ-XRF approach is the pixel-size resolution of the beam spot used, some tenths of µm. This is several orders of magnitude larger than nanometer-sized soil colloids, known for their high reactivity with metal elements and suspected to be largely involved in the transfer of metal pollutants in soils [7,42]. Hence, metal distributions related to colloidal clays, iron oxides and/or humic substances may be assessed by µ-XRF only when these colloids accumulate in sub-millimeter-sized characteristic pedofeatures, such as distinct clay, iron or manganese coatings or in organic matter precipitates [15,17,18]. Our sub-millimeter to

micrometer-scale approach on pedofeatures provided valuable insight into contaminant dynamics in soils and thus represents an essential step prior to molecular-scale studies [21], at the halfway between field survey and the solid–liquid interface level.

4.2. Soil Processes and Metal Accumulations

4.2.1. Neoformation of Metal-Phases

The presence of distinct trace-metal phases was rarely reported in agricultural soils, because it requires specific conditions involving oversaturation of a pure solution or geomicrobial processes [43]. In the surface horizon of Site 1, contaminated by temporary industrial waste disposal, the occurrence of small spherical crystals with large contents of Zn, Pb, Cu, Fe, Mn and Ca, in and around weathered industrial waste fragments, gave evidence for at least temporary conditions of an oversaturated soil solution. Alternating drying and wetting cycles at the soil surface lead to the co-precipitation of neoformed composite metalliferous phases (Figure 1). The recurrent presence of small spherulites on large POM fragments suggests that organic surfaces may enhance their formation, likely favored by microbial activity. Clusters of yellowish spherulites mixed with quartz grains in the groundmass may result from mechanical disturbance by annual plowing practices. The dense Ap2 horizon reduces the percolation of the soil solution, prolonging the contact time with weathering waste and leading to concentrated metal loads in the soil solution before arrival in the underlying B horizons. When a saturated or viscous solution enters a well-aerated, porous environment, spherulite crystallization can occur [34]. Such newformation was dominantly observed in and closely around macropores and occasionally as individual, reddish iron-rich spherulites randomly distributed in the soil groundmass. Their occurrence until about 70-cm depth and their location, primarily related to large voids, suggested that preferential flow of soil water that bypasses a large part of the groundmass, plaid an important role in the transfer of trace metals. Similar neoformed crystals, but composed of Cu carbonate, were described as greenish spherulites [44] in coarse textured calcareous C horizons of glacial till, underlying a dense Bt horizon in a soil polluted by As, Cr and Cu. Their formation was attributed to slow percolation of a saturated soil solution trough the low-permeable clay rich B horizon and precipitation of dissolved matter after its abrupt arrival in the aerated C horizon.

4.2.2. Accumulation of TM by Soil Constituents

In surface horizon samples of both study sites, μ-XRF revealed contrasting metal-distribution patterns with metal-accumulation hotspots occurring in a groundmass with moderate, diffuse concentrations. Phosphates and undecayed, or partially decomposed plants tissues were revealed as strong metal-retaining constituents [37,45–47]. In our work, strong correlations of Zn and Pb with Fe and Mn were particularly observed for iron-phosphates. The frequent observation of iron phosphates in metal-contaminated soils questions about a possible role of heavy metals on reducing P-availability. Particulate organic matter particles isolated by physical fractionation in water from surface samples collected in metal contaminated agricultural soils [48] displayed very large metal concentrations [36,40,41,49]. With time, preferential microbiological degradation of little contaminated POM parts and/or increased reactivity of organic cellular structures may enhance a relative concentration of heavy metals in smaller POM parts, finally leading to a mutual metal–carbon sequestration [36]. Such a process of formation of long-term stable organo-metal complexes would agree with emergent views on the stabilization and chemical recalcitrance of organic matter (e.g., [50,51]). Individual finely divided constituents, such as clay minerals, iron and manganese oxyhydroxydes and humic acids develop large surface reactivity and ensure a large part of metal retention in many soils. However, due to their small size, these compounds are out of scope in our study approach. However, in many contaminated surface horizons, in terms of metal stocks, the finest soil fractions (<20 μm, or <2 μm) generally represent the main proportion of the total metal load.

4.2.3. Metal Transport via the Soil Solution in the Soil Profile

The downward migration of dissolved TM can occur either slowly, by diffusion, or more rapidly via the transport of the soil solution. In particular, preferential flow in soil cracks and large biopores may explain the presence of mobile and little mobile metal pollutants at a considerable soil depth [52,53]. In the soil solution, TM may exist in the form of hydrated cations but also in colloidal form as organic or inorganic complexes, or bound to suspended solids [54]. Detailed in situ lysimeter study was undertaken during three years in five soils under different land use in the area of Site 1, aiming to assess the chemical speciation of TM in gravitational soil water percolating the soils through successive soil horizons [55]. That work showed that Zn and Cd were always predominantly found in dissolved forms and as free ions or labile complexes [42]. On the contrary, Pb was quasi-exclusively in colloidal forms, associated with composite colloids, often Fe- oxides. In addition, a substantial proportion of Pb in solution was present as stable complexes, or labile complexes with slow dissociation kinetics, explaining low interaction with reactive soil constituents during percolation of the soil solution through clay-rich Bt horizons.

Such contrasting chemistry for Zn and Pb in the soil solution, explained to a large part their diverging microscale distributions observed in the study soil profiles of Site 1: free Zn^{2+} was intercepted in B horizons by negatively charged surfaces of soil compounds in iron- and clay coatings and in manganese nodules (Figure 3e,g–i; Tables 1 and 3). However, Pb was not detected by µ-XRF in subsurface horizons between 30 and 120 cm soil depth. However, between 120 and 150 cm, in the C1g horizon, pure iron coatings show remarkably high Pb/Fe correlation (ρ = 0.78) for such great depth (Figure 3i, Table 3), whereas abruptly no more correlation was observed for Zn neither with Fe nor Mn. Obviously, all mobile Zn has been intercepted in the overlying B horizons. The sudden accumulation of Pb was ascribed to contrasting redox conditions resulting from the fluctuating water table, thus constraining Pb-bearing iron colloidal phases to precipitate. Several points attest for a contemporary origin of the pure iron coatings by precipitating colloidal iron from the soil solution in voids: (i) a sharp boundary with underlying clay coatings points to a recent process of iron illuviation via voids rather than iron segregation out of the groundmass; (ii) no Pb accumulation was observed in hypo- and quasi-iron coatings related to gleyic properties in the C horizon; and (iii) the absence of Zn/Pb correlation also corroborates distinct Zn and Pb dynamics at great depth.

For Site 2, indications for colloidal transport were given by Pb and Cu accumulations occurring at the contact with the carbonate parent material (Figure 6k), presumably due to abruptly rising of the pH, constraining organic colloids and iron-rich colloids to precipitate. The dark brown, dusty clay coatings typically occur in E and upper Bt horizons of Luvisols, below the plow-layer. Such coatings represent the youngest phase of illuviation of finely divided groundmass material from the Ap horizon, including dispersed organic matter and indicate recent land use changes [56].

4.2.4. Biotic Metal Accumulation

Abundant fungal activity in deep soil horizons is scarcely mentioned. In the wastewater irrigated soil, strongly contrasting hydrodynamic conditions occurring at the boundary between the low permeable clay-rich Bt horizon and the aerated E or C horizons, fungal tissues, dark opaque sclerotized material and manganese oxide coatings were abundant. Such dark opaque features were reported as manganiferous compounds originating from fungal Mn-reducing activity hot-spots in soils with temporarily anoxic conditions [39]. The microorganisms translocate soluble Mn^{2+} from reduced anoxic to aerobic soil environments and oxidize it to low- or non-soluble Mn^{3+} or Mn^{4+} compounds [57]. These features demonstrated a preferential strong correlation for Mn with Zn and lower correlation between Zn and Fe (Table 4). Such findings underline the key role of microbial-mediated processes controlling metal transfer and localized accumulations in sub-surface horizons.

4.2.5. Uncommon Soil Processes in Humid Temperate Climatic Conditions

One century of wastewater discharge activity on Luvisol with sandy-textured surface horizons had consequences on soil development that are not so common in the temperate climatic conditions of northern France. Due to strongly contrasting soil moisture conditions, i.e., waterlogging subsequent to wastewater flooding events and subsequent rapid and strong drying of the coarse-sand textured surface horizon, upward moving of soil water from the clay rich Bt horizon upwards in the E horizon leads to the formation of thin, reddish-brown, clay-iron bands. Their formation is presumably related to capillary rising of soil water and suspended fine material from the Bt horizons, consistent with: (1) their morphology of bow-like bands that developed restrictively above thick clay bodies and anchored at the borders of the cryoturbation structures; and (2) their maximal height of about 10–15 cm above the top of the Bt horizon in agreement with literature data for sandy soils [58]. In these pedofeatures, high correlation is observed for Zn and Mn, and low correlation for Zn and Fe (Table 4). Such repetitive alternating redox conditions at the contact between the E and Bt horizon have led to ferrolysis, with evidence for clay destruction enhancing temporary local soil acidification, the formation of Al-hydroxyl interlayered clay, iron reduction and iron redistribution [17,18]. In the E-Bt transition horizon and in the upper part of the Bt horizon, pure iron hydroxide coatings were frequently observed and contained high amounts of Zn, Pb and some Cu, but not Mn (Table 3). Such distributions were consistent with co-precipitation of iron liberated by hydromorphic clay degradation in the E/Bt horizon and dissolved or colloidal-bound migrating trace metals.

4.3. Heterogeneous TM Distribution Patterns in Soils Call for Adapted Sampling Strategies

After arrival of metal pollution on, and its incorporation within the soil surface layer, the competition between reactive soil constituents and the initial metal-bearing mineral or organic phases leads to redistribution of TM and an increasingly diversified metal speciation. Organic residues in litter layers or coarse and fine POM fragments, occurring abundantly in A horizons of metal polluted soils, may demonstrate very large TM concentrations [12,36,41], but in terms of metal stocks, the finest soil fractions most often include the main metal loads [26]. With time, metal pollution will be incorporated differently in agricultural arable land and grassland soils: a progressively decreasing of TM concentrations with depth under pasture due to enhanced biological (earthworm) activity versus a strong discontinuous TM profile in cultivated soils due to fertilization and mechanization practices that lead to a fairly constant TM profile in the plow layer that contrasts with the subsurface horizons [25,26]. Moreover, in acid forest soils, a substantial proportion of more mobile metals, such as Zn and Cd can be "rapidly" leached out of the soil profile, within a time span of several decades [12,24]. Finally, for wastewater pollution, the example of contrasting physicochemical conditions in the Ap horizons, with respect to underlying horizons (Figure 5) showed that metal retention is controlled at the horizon boundary within a distance of some tenths of micrometers only.

At depth, different soil processes resulting from local pedoclimatic conditions and often amplified by anthropogenic activities control the incorporation dynamics and fate of metal pollutants in subsurface horizons, sometimes until great depth. Although affected by strongly diverging polluting practices, both soils exhibited fairly comparable metal accumulations in ancient or contemporary pedofeatures, related to percolating soil solution in large pores. From there, soil water and solutes may diffuse into the bulk soil and disseminate TM among the fine groundmass. In all pedofeatures, Zn and/or Mn were clearly present, and their correlation with at least one TM fairly systematically exceeded 0.9 (Tables 3 and 4). Iron, Mn and Ca are major soil elements, indicators for many soil processes and mechanism, and omnipresent in many pedofeatures. Both Fe and Mn-oxyhydroxides are strong natural pigments, and their localized concentrations in the soil profile are helpful to pedologists for identifying in the field the soil processes that are active but also the impacts of environmental and/or human constraints. Therefore, examination of spatial distribution of Fe and Mn in subsurface horizons may help to get an early insight in metal dynamics in contaminated soils. Similarly, field survey of such Fe and Mn distribution should guide field sampling instead of systematic soil depth

sampling. Thus, the clear lead accumulation in neoformed iron coatings in the C1g horizon (Figure 1i, Table 3) could not be viewed from Pb concentrations analyzed on bulk depth sampling (Table 1): 11.9 g/kg of Pb at 120–150 cm depth in the C1g horizon with many Pb-bearing iron coatings and 12.3 g/kg of Pb between 80 and 120 cm in the overlying BC horizon, where no Pb accumulations were observed.

As a general rule for relevant sampling of contaminated soils, first a detailed field survey of polluted and unpolluted soil profiles must be performed, on the condition that they display comparable nature, formation and behavior conditions. Such a first step is essential for identifying subtle macromorphological nuances between equivalent soil horizons (thickness, structure, mottling or color). It provides a first impression of possible effects of anthropogenic polluting activities. Based on that information, soil sampling strategy must then be adapted so that the collection of samples respects pedological horizon boundaries and/or selected depths according morphological criteria. Relevant environmental risk assessment of contaminant dynamics in soil profiles requires sampling strategies based on pedological expertise that respect soil horizon boundaries and/or soil morphological criteria and hence, the use of systematic soil-depth sampling in naturally-developed soils must be banished.

5. Conclusions

Combined optical microscopy and submicroscopic analytical techniques applied on undisturbed samples from A, B and C horizon of contaminated soils offers a relevant focus—at a study scale halfway between the field and the solid–liquid interface—on the effects of physical, chemical and biological processes that control contaminant dynamics. For surface horizons of agricultural soils, such approach revealed strongly contrasting metal concentrations between, on the one hand, TM hotspots coinciding with: (1) initial metalliferous phases deriving from anthropogenic polluting activities; (2) highly reactive TM-hosting soil constituents (POM, phosphates, oxides); and (3) localized neoformed trace-metal rich crystals resulting from co-precipitation out of a temporary oversaturated soil solution, and, on the other hand, more moderate metal concentrations, diffusely distributed according the specific c/f related distribution pattern. Despite clear lower TM concentrations, in terms of metal stocks, the fine plasma may represent the major metal-binding soil fraction in many contaminated surface soils. In subsurface horizons, consistent TM-accumulations predominantly occurred in pedofeatures (dust, clay, iron, and manganese coatings) related to characteristic soil processes in B and C horizons. Their location in, or close to, large voids indicates a migration of TM mainly via the soil solution and the interception of dissolved TM by reactive phases, or (co)-precipitation of TM-bearing colloids when soil conditions (pH, Eh) suddenly change. Pedofeatures were often materialized by consistent Fe and/or Mn concentrations, as confirmed by outstandingly high correlation ($\rho > 0.8$) between Zn or Pb with Fe and/or Mn for 9 out of 13 studied pedofeatures in horizons below the Ap layer (Tables 3 and 4), until great depths (>1.5 m). In the field, pedologists are experienced in "reading" the distribution of iron and manganese pigments to identify active or past soil processes and to localize the related pedofeatures. Sampling of undisturbed soil samples is essential for preserving the marks, structures and contaminant redistributions resulting from soil processes, and their examination is helpful to agronomists, environmental technicians and stakeholders for making more relevant decisions with respect to future management of contaminated soils. Hence, pedological expertise is a prerequisite when sampling contaminated soils for valuable environmental risk assessment studies, whereas a systematic soil-depth sampling strategy will easily overlook preferential contaminant accumulations controlled by soil processes.

Acknowledgments: The authors acknowledge financial support from the French Ministry of Environment (MTES), from Conseil Régional de l'Île de France (CRIdF), Conseil Général du Val d'Oise (CG95), Agence de l'Eau Seine-Normandie (AESN) (AESN-031300) and Syndicat Interdépartemental pour l'Assainissement de l'Agglomération Parisienne (SIAAP). The authors are also grateful to the three anonymous referees for their comments and helpful suggestions.

Author Contributions: Folkert van OORT conseived and designed the experiments; Sophie Leguédois, Jérôme Labanowski and Folkert van OORT performed the experiments and analyzed the data; Eddy Foy supervised the µ-XRF experiments, Toine Jongmans supervised the micromorphology study; Folkert van OORT, Sophie Leguédois, Jérôme Labanowski, Eddy Foy, and Toine Jongmans wrote the paper.

Conflicts of Interest: The authors declare no conflict of interest.

References

1. Ettler, V. Soil contamination near non-ferrous metal smelters: A review. *Appl. Geochem.* **2016**, *64*, 56–74. [CrossRef]
2. Adriano, D.C. Biogeochemical processes regulating metal behavior. In *Trace Elements in Terrestrial Environments—Biogeochemistry, Bioavailability, and Risks of Metals*; Adriano, D.C., Ed.; Springer: New York, NY, USA, 2001; ISBN 978-1-4684-9505-8.
3. Sobanska, S.; Ricq, N.; Laboudigue, A.; Guillermo, R.; Brémard, C.; Laureyns, J.; Merlin, J.C.; Wignacourt, J.P. Microchemical investigations of dust emitted by a lead smelter. *Environ. Sci. Technol.* **1999**, *33*, 1334–1339. [CrossRef]
4. Lamy, I.; van Oort, F.; Dère, C.; Baize, D. Use of major- and trace-element correlations to assess metal migration in sandy Luvisols irrigated with wastewater. *Eur. J. Soil Sci.* **2006**, *57*, 731–740. [CrossRef]
5. Stoops, G. *Guidelines for Analysis and Description of Soil and Regolith Thin Sections*; SSSA Inc.: Madison, WI, USA, 2003; ISBN 0-8911-842-8.
6. Violante, A.; Cozolino, V.; Perelomov, L.; Caporale, A.G.; Pigna, M. Mobility and bioavailability of heavy metals and metalloids in soil environments. *J. Soil Sci. Plant Nutr.* **2010**, *10*, 268–292. [CrossRef]
7. Kretzschmar, R.; Borkovec, M.; Grolimund, D.; Elimelech, M. Mobile subsurface colloids and their role in contaminant transport. *Adv. Agron.* **1999**, *66*, 121–193. [CrossRef]
8. Jacobson, A.R.; Dousset, S.; Andreux, F.; Baveye, P.C. Electron microprobe and synchrotron X-ray fluorescence mapping of the heterogeneous distribution of copper in high-copper vineyard soils. *Environ. Sci. Technol.* **2007**, *41*, 6343–6349. [CrossRef] [PubMed]
9. Scarciglia, F.; Barca, D.; De Rosa, R.; Pulice, I. Application of laser ablation ICP-MS and traditional micromorphological techniques to the study of an Alfisol (Sardinia, Italy) in thin sections: Insights into trace element distribution. *Geoderma* **2009**, *152*, 113–126. [CrossRef]
10. Scarciglia, F.; Barca, D. A powerful tool for assessing distribution and fate of potentially toxic metals (PTMs) in soils: Integration of laser ablation spectrometry (LA-ICP-MS) on thin sections with soil micromorphology and geochemistry. *Environ. Sci. Pollut. Res.* **2017**, *24*, 9776–9790. [CrossRef] [PubMed]
11. Zampella, M.; Adamo, P.; Caner, L.; Petit, S.; Righi, D.; Terribile, F. Chromium and copper in micromorphological features and clay fractions of volcanic soils with andic properties. *Geoderma* **2010**, *157*, 185–195. [CrossRef]
12. Baize, D.; van Oort, F. Potentially Harmful Elements in Forest Soils. A Pedological Viewpoint. In *Potential Harmful Elements, Environment and Human Health*; Bini, C., Bech, J., Eds.; Springer Science + Business Media: Dordrecht, The Netherlands, 2014; pp. 151–198. ISBN 978-94-017-8964-6.
13. Stoops, G.; Marcellino, V.; Mees, F. *Interpretation of Micromorphological Features of Soils and Regoliths*; Elsevier: Amsterdam, The Netherlands, 2010; 720p, ISBN 978-0-444-53156-8.
14. Leguédois, S.; van Oort, F.; Jongmans, A.G.; Chevallier, P. Morphology, chemistry and distribution of neoformed mineral species in agricultural land affected by metallurgical point-source pollution. *Environ. Pollut.* **2004**, *130*, 135–148. [CrossRef] [PubMed]
15. Van Oort, F.; Jongmans, A.G.; Citeau, L.; Lamy, I.; Chevallier, P. Microscale Zn and Pb distribution patterns in subsurface soil horizons: An indication for metal transport dynamics. *Eur. J. Soil Sci.* **2006**, *57*, 154–166. [CrossRef]
16. Van Oort, F.; Labanowski, J.; Jongmans, T.; Thiry, M. Le devenir des polluants métalliques dans les sols: Révélateur d'impacts de l'activité humaine sur la pédogenèse? *Etude Gest. Sols* **2007**, *14*, 287–303.
17. Van Oort, F.; Jongmans, A.G.; Lamy, I.; Baize, D.; Chevallier, P. Impacts of long-term wastewater irrigation on the development of sandy Luvisols: Consequences for metal pollutant distributions. *Eur. J. Soil Sci.* **2008**, *59*, 925–938. [CrossRef]

18. Van Oort, F.; Thiry, M.; Foy, E.; Fujisaki, K.; Delarue, G.; Dairon, R.; Jongmans, A.G. Impacts of one century of wastewater discharge on soil transformation through ferrolysis and related metal pollutant distributions. *Sci. Total Environ.* **2017**, *590–591*, 1–13. [CrossRef] [PubMed]
19. Neaman, A.; Martínez, C.E.; Trolard, F.; Bourrié, G. Trace element associations with Fe- and Mn-oxides in soil nodules: Comparison of selective dissolution with electron probe microanalysis. *Appl. Geochem.* **2008**, *23*, 778–782. [CrossRef]
20. Huot, H.; Simonnot, M.O.; Watteau, F.; Marion, P.; Yvon, J.; De Donato, P.; Morel, J.L. Early transformation and transfer processes in a Technosol developing on iron industry deposits. *Eur. J. Soil Sci.* **2014**, *65*, 470–484. [CrossRef]
21. Kelly, S.D.; Hesterberg, D.; Ravel, B. Analysis of soils and minerals using X-ray absorption spectroscopy. In *Methods of Soil Analysis, Part 5—Mineralogical Methods*; Ulery, A.L., Drees, L.R., Eds.; SSSA Inc.: Madison, WI, USA, 2008; pp. 387–463. ISBN 978-0-89118-746-9.
22. Sterckeman, T.; Douay, F.; Proix, N.; Fourrier, H.; Perdrix, E. Assessment of the contamination of cultivated soils by eighteen trace elements around smelters in the north of France. *Water Air Soil Pollut.* **2002**, *135*, 173–194. [CrossRef]
23. Thiry, M.; Huet-Taillanter, S.; Schmitt, J.M. La friche industrielle de Mortagne-du-Nord (59). I. Prospection du site, composition des scories, hydrologie et estimation des flux. *Bull. Soc. Géol. Fr.* **2002**, *173*, 369–381. [CrossRef]
24. Van Oort, F.; Thiry, M.; Jongmans, A.G.; Bourennane, H.; Cambier, P.; Lamy, I.; Citeau, L.; Nahmani, J. Pollutions métalliques : Distributions hétérogènes du Zn, Pb, Cd, et Cu et relations avec l'usage des sols. In *Contaminations Métalliques des Agrosystèmes et Écosystèmes Péri-Urbains*; Cambier, P., Schvartz, C., van Oort, F., Eds.; Éditions Quæ: Versailles, France, 2009; pp. 15–44. ISBN 978-2-7592-0275-1.
25. Fernandez, C.; Labanowski, J.; Cambier, P.; Jongmans, A.G.; van Oort, F. Fate of airborne pollution in soils as related to agricultural management: 1. distributions of Zn and Pb in soil profiles. *Eur. J. Soil Sci.* **2007**, *58*, 547–559. [CrossRef]
26. Fernandez, C.; Labanowski, J.; Jongmans, T.; Bermond, A.; Cambier, P.; Lamy, I.; van Oort, F. Fate of airborne metal pollution in soils as related to agricultural management: 2. Assessing the role of biological activity in micro-scale Zn and Pb distributions in A, B and C horizons. *Eur. J. Soil Sci.* **2010**, *61*, 514–524. [CrossRef]
27. IUSS Working Group WRB. World Reference Base for Soil Resources. In *International Soil Classification System for Naming Soils and Creating Legends for Soil Maps*; World Soil Resources Reports No. 106; FAO: Rome, Italy, 2014; ISBN 978-92-5-108369-7.
28. Toze, S. Reuse of effluent water—Benefits and risks. *Agric. Water Manag.* **2006**, *80*, 147–159. [CrossRef]
29. Ternes, T.A.; Bonerz, M.; Herrmann, N.; Teiser, B.; Andersen, H. Irrigation of treated wastewater in Braunschweig, Germany: An option to remove pharmaceuticals and musk fragrances. *Chemosphere* **2007**, *66*, 894–904. [CrossRef] [PubMed]
30. Védry, B.; Gousailles, M.; Affholder, M.; Lefaux, A.; Bontoux, J. From sewage water treatment to wastewater reuse. One century of Paris sewage farms history. *Water Sci. Technol.* **2001**, *43*, 101–107. [PubMed]
31. Tamtam, F.; van Oort, F.; LeBot, B.; Dinh, T.; Mompelat, S.; Chreveuil, M.; Lamy, I.; Thiry, M. Assessing antibiotic contamination in metal contaminated soils four years after cessation of long-term wastewater irrigation. *Sci. Total Environ.* **2011**, *409*, 540–547. [CrossRef] [PubMed]
32. Thiry, M.; van Oort, F.; Thiesson, J.; van Vliet-Lanoë, B. Periglacial morphogenesis in the Paris Basin: Insight from geophysical prospection and impacts for the fate of soil pollution. *Geomorphology* **2013**, *197*, 34–44. [CrossRef]
33. FitzPatrick, E.A. *Soil Microscopy and Micromorphology*; Wiley: Chichester, UK, 1993; 304p, ISBN 0-471-93859-9.
34. Canti, M.G. An investigation of microscopic calcareous spherulites from herbivore dungs. *J. Archaeol. Sci.* **1997**, *24*, 219–231. [CrossRef]
35. Bullock, P.N.; Fédoroff, N.; Jongerius, A.; Stoops, G.; Tursina, T. *Handbook for Soil Thin Section Description*; Waine Research Publications: Albrighton, UK, 1985; 152p, ISBN 09051847-09-2.
36. Labanowski, J.; Sebastia, J.; Foy, E.; Jongmans, A.G.; Lamy, I.; van Oort, F. Fate of metal-associated POM in a soil under arable land use contaminated by metallurgical fallout in northern France. *Environ. Pollut.* **2007**, *149*, 59–69. [CrossRef] [PubMed]
37. Fendorf, S.; La Force, M.J.; Li, G. Temporal changes in soil partitioning and bioaccessibility of arsenic, chromium and lead. *J. Environ. Qual.* **2004**, *33*, 2049–2055. [CrossRef] [PubMed]

38. Brinkman, R. Ferrolysis, a hydromorphic soil forming process. *Geoderma* **1970**, *3*, 199–206. [CrossRef]
39. Thompson, I.A.; Huber, D.M.; Guest, C.A.; Schulze, D.G. Fungal manganese oxidation in a reduced soil. *Environ. Microbiol.* **2005**, *7*, 1480–1487. [CrossRef] [PubMed]
40. Flores-Velez, L.M.; Ducaroir, J.; Jaunet, A.M.; Robert, M. Study of the distribution of copper in an acid sandy vineyard soil by three different methods. *Eur. J. Soil Sci.* **1996**, *47*, 523–532. [CrossRef]
41. Besnard, E.; Chenu, C.; Robert, M. Influence of organic amendments on copper distribution among particle-size and density fractions in Champagne vineyard soils. *Environ. Pollut.* **2001**, *112*, 329–337. [CrossRef]
42. Citeau, L.; Lamy, I.; van Oort, F.; Elsass, F. Colloidal facilitated transfer of metals in soils under different land use. *Colloids Surf. A* **2003**, *217*, 11–19. [CrossRef]
43. Banfield, J.F.; Nealson, K.H. *Geomicrobiology: Intercations between Microbes and Minerals*; Reviews in Mineralogy; Mineralogical Society of America: Chantilly, VA, USA, 1997; Volume 35, 448p, ISBN 978-0939950454.
44. Lund, U.; Fobian, A. Pollution of two soils by arsenic, chromium and copper, Denmark. *Geoderma* **1991**, *49*, 83–103. [CrossRef]
45. Cotter-Howells, J.D.; Caporn, S. Remediation of contaminated land by formation of heavy metal phosphates. *App. Geochem.* **1996**, *11*, 335–342. [CrossRef]
46. Hettiarachchi, G.M.; Pierzynski, G.M. In situ stabilization of soil lead using phosphorus and manganese oxide: Influence of plant growth. *J. Environ. Qual.* **2002**, *31*, 564–572. [CrossRef] [PubMed]
47. Magdi Selim, H. *Phosphates in Soil. Interaction with Micronutriments, Radionuclides and Heavy Metals*; CRC Press, Taylor & Francis Group: Boca Raton, FL, USA, 2015; 381p, ISBN 978-1-4822-3679-8.
48. Christensen, B.T. Physical fractionaton of soil and structural and functional complexity in organic matter turnover. *Eur. J. Soil Sci.* **2001**, *52*, 345–353. [CrossRef]
49. Ducaroir, J.; Lamy, I. Evidence of trace metal association with soil organic matter using particle size fractionation after physical dispersion treatment. *Analyst* **1995**, *120*, 741–745. [CrossRef]
50. Lehmann, J.; Kleber, M. The contentious nature of soil organic matter. *Nature* **2015**, *528*, 60–68. [CrossRef] [PubMed]
51. Mikutta, R.; Kleber, M.; Torn, M.S.; Jahn, R. Stabilization of soil organic matter: Association with minerals or chemical recalcitrance? *Biogeochemistry* **2006**, *77*, 25–56. [CrossRef]
52. Bundt, M.; Albrecht, A.; Froidevaux, P.; Blaser, P.; Flühler, H. Impact of preferential flow on radionuclide distribution in soil. *Environ. Sci. Technol.* **2000**, *34*, 3895–3899. [CrossRef]
53. Knechtenhofer, L.A.; Xifra, I.O.; Scheinost, A.C.; Flühler, H.; Kretzschmar, R. Fate of heavy metals in a strongly acidic shooting-range soil: Small-scale metal distribution and its relation to preferential water flow. *J. Plant Nutr. Soil Sci.* **2003**, *166*, 84–92. [CrossRef]
54. Tack, F.M.G. Trace elements: General soil chemistry, principles and processes. In *Trace Elements in Soils*; Hooda, P.S., Ed.; Wiley: Chichester, UK, 2010; pp. 9–39. ISBN 978-1-045-16037-7.
55. Citeau, L. Etude des Colloïdes Naturels Circulant dans les eaux Gravitaires de sols Contaminés: Nature des Colloïdes et Réactivité vis-à-vis des Métaux. Ph.D. Thesis, 2004, INAPG, Paris, France.
56. Kühn, P.; Aguilar, J.; Miedema, R. Textural pedofeatures and related horizons. In *Interpretation of Micromorphological Features of Soils and Regoliths*; Stoops, G., Marcelino, V., Mees, F., Eds.; Elsevier: Amsterdam, The Netherlands, 2010; pp. 217–250. ISBN 978-0-444-53156-8.
57. Ehrlich, H.L. Geomicrobiology: Its significance for geology. *Earth Sci. Rev.* **1998**, *45*, 45–60. [CrossRef]
58. Soltner, D. *Les Bases de la Production Végétale 1. Le sol*, 12th ed.; Sciences et Techniques Agricoles: Paris, France, 1983.